Impact of ENSO on SST Variability in the North Pacific and North Atlantic: Seasonal Dependence and Role of Extratropical Sea–Air Coupling

NGAR-CHEUNG LAU AND MARY JO NATH

NOAA/Geophysical Fluid Dynamics Laboratory, Princeton University, Princeton, New Jersey

(Manuscript received 13 July 2000, in final form 2 January 2001)

ABSTRACT

The influences of El Niño–Southern Oscillation (ENSO) events in the tropical Pacific on interannual variability of the coupled ocean–atmosphere systems in the North Pacific and North Atlantic have been studied using a suite of experiments with a rhomboidal 30-wavenumber, 14-layer general circulation model (GCM). Observed month-to-month fluctuations of the sea surface temperature (SST) in the tropical Pacific during the 1950–95 period were prescribed as the lower boundary condition for the GCM. The SST conditions outside of the tropical Pacific were predicted by a simple ocean mixed layer model with a constant depth. Four independent integrations under this ''Tropical Ocean–Global Atmosphere–Mixed Layer (TOGA-ML)'' scenario were conducted.

Both observational and model results indicate that the imposed ENSO forcing during midwinter is accompanied by prominent atmospheric circulation changes over the North Pacific and Atlantic. These teleconnection patterns in turn alter the heat exchange across the local sea–air interface. The extratropical SST anomalies generated by this ''atmospheric bridge'' mechanism typically attain maximum amplitudes in late winter or early spring.

Detailed diagnoses of the monthly evolution of the surface heat budget during ENSO episodes at selected sites have been performed. The simulated SST response exhibits a 1–2 month delay relative to temperature changes in the overlying atmosphere. This lag relationship is associated with a polarity change of sea-to-air gradients in anomalous temperature and water vapor mixing ratio in late winter. From late autumn through midwinter, the action of the climatological wind on these gradients results in enhancement of the developing SST anomalies. In the months thereafter, the reversed gradients lead to attenuation of the SST signal. Shortwave radiative fluxes associated with variations in cloud cover play an important role in SST variability at some of the subtropical sites.

The nature of sea–air feedbacks in the extratropics has been studied by contrasting the output from the TOGA-ML experiment and from another ''TOGA'' experiment in which two-way interactions between the atmosphere and ocean outside of the tropical Pacific were eliminated. Incorporation of sea–air coupling in TOGA-ML is seen to enhance the persistence of the ENSO-related atmospheric anomalies in the extratropics through late winter and early spring. Comparison with results from previous studies on midlatitude sea–air interactions suggests that part of the atmospheric signal in TOGA-ML may be attributed to forcing from extratropical SST anomalies produced by the atmospheric bridge mechanism.

1. Introduction

There is now abundant observational evidence on the occurrence of well-defined circulation anomalies in the extratropical atmosphere during El Niño–Southern Oscillation (ENSO) episodes (e.g., see the recent review by Trenberth et al. 1998). Weare et al. (1976), Hsiung and Newell (1983), and Pan and Oort (1990) have also reported that ENSO events are accompanied by marked changes in the midlatitude sea surface temperature (SST) patterns in the North Pacific and North Atlantic. The concept of an ''atmospheric bridge'' has been invoked in various investigations (e.g., Alexander 1990, 1992a,b; Luksch and von Storch 1992; Lau and Nath 1996) to interpret these sets of relationships between tropical ENSO phenomena and interannual variability of the ocean–atmosphere system in the temperate zone. These studies suggest that the following chain of processes may be at work: the extratropical atmosphere responds to perturbed tropical forcings during ENSO events; the resulting midlatitude atmospheric anomalies then exert local influences on the underlying ocean through alterations of energy and momentum fluxes across the sea–air interface, thereby generating extratropical SST anomalies. In the above scenario, the atmosphere essentially serves as an intermediary (or ''bridge'') linking ENSO-related SST anomalies in the tropical Pacific to oceanic variations in the extratropics.

In our previous study on this subject (Lau and Nath 1996; hereinafter referred to as LN96), different aspects of the atmospheric bridge mechanism have been studied using a variety of model experiments. In all of these

Corresponding author address: Dr. Ngar-Cheung Lau, NOAA/Geophysical Fluid Dynamics Laboratory, Princeton University, P.O. Box 308, Princeton, NJ 08542.
E-mail: gl@gfdl.noaa.gov

experiments, the month-to-month SST variations in the tropical Pacific as observed during the past several decades were prescribed at the bottom boundary of a low-resolution atmospheric general circulation model (GCM). The interactions between the wintertime GCM responses in the Northern Hemisphere extratropics with the underlying oceans were then investigated using a simple model of the oceanic mixed layer with a constant depth. The experimental designs ranged in complexity from one-way atmospheric driving of the mixed layer, to linear damping of the atmospheric forcing due to fluctuations of the mixed layer temperature, and to full two-way coupling between the atmospheric GCM and the mixed layer. The results from these experiments support the notion that some of the prominent patterns of midlatitude SST variability on interannual timescales are primarily forced by ENSO-related atmospheric circulation anomalies. Some evidence has also been shown in LN96 on the presence of positive feedbacks of the midlatitude SST signals on the atmospheric driving. However, the model diagnoses performed by Alexander (1992a,b) and Bladé (1999) suggest that such sea–air feedbacks may actually be negative.

The present study is a continuation of the investigation initiated in LN96. We now focus on a new set of experiments using a GCM with a twofold increase in spatial resolution [i.e., rhomboidal truncation at 30-wavenumber (R30) versus 15-wavenumber (R15) in LN96]. The higher-resolution model provides a better simulation of ENSO-related changes in tropical heat sources and sinks, and in activity of extratropical transient disturbances. Accordingly, the amplitudes of the extratropical atmospheric responses appearing in the R30 runs are more realistic than the R15 results (see discussion in section 6). The improved performance of the R30 model motivates us to conduct further analyses of the detailed seasonal characteristics of the atmospheric bridge mechanism, the impact of this mechanism on sea–air coupling in both the North Pacific and North Atlantic, and contributions of various processes to the heat budget of the mixed layer at various ocean sites during prominent ENSO episodes. A stronger attempt is also made in this study to compare the model results with available observations. The scope of the present work is considerably broader than that of LN96, which is primarily focused on simulation of the bridge linking the tropical and extratropical Pacific during the winter season only.

A description of the model tools, experimental design and observational datasets is given in section 2. Simulated and observed aspects of the impact of ENSO on ocean–atmosphere variability in the North Pacific are presented in section 3. The corresponding results on ENSO connections with the North Atlantic are shown in section 4. Various facets of extratropical sea–air coupling that are pertinent to the atmospheric bridge mechanism are considered in section 5. The essential findings are summarized and discussed in section 6.

2. Model and observational datasets

The spectral R30 GCM used for this study has been developed and maintained by the Climate Dynamics Project at the Geophysical Fluid Dynamics Laboratory. It has an equivalent horizontal resolution of 3.75° and ~2.2° in the zonal and meridional directions, respectively. Vertical variations are represented at 14 sigma levels. Boundary conditions and physical processes incorporated in this model include land–sea contrast, large-scale orography, a full hydrological cycle, predicted cloud cover, radiative transfer and gravity wave drag. Further details of the model numerics and physics were described in Gordon and Stern (1982) and Broccoli and Manabe (1992). The atlas of Alexander and Scott (1995) contains a comprehensive collection of climatological statistics of this model.

Two types of SST forcing scenarios were considered in this study. In the first experiment [Tropical Ocean–Global Atmosphere (TOGA)], observed month-to-month SST variations were inserted at the lower boundary within the tropical Pacific between ~25°S and ~25°N. Climatological SST values were prescribed at all remaining ocean grid points. The second experiment [referred to as TOGA–Mixed Layer (TOGA-ML)] was similar to TOGA, except that the SST conditions at all ice-free maritime sites outside the tropical Pacific were predicted using a simple ocean mixed layer model. The latter model computed temperature changes in a water column due to variations in heat and radiative fluxes at the sea–air interface. The depth of the mixed layer was fixed at 50 m. Interactions between mixed layers at neighboring grid points were not considered. The heat flux adjustment procedure described by Manabe et al. (1991) has been used to ensure that the climatological evolution of the mixed layer temperature is in agreement with observations. Both the TOGA and TOGA-ML experiments were conducted for the 1950–95 period. The interannually varying tropical Pacific SST conditions in this period were based on the observations compiled by Smith et al. (1996) using a reconstruction algorithm based on empirical orthogonal functions. Four parallel integrations were performed for each of the TOGA and TOGA-ML scenarios, with each run being initiated from an independent set of atmospheric conditions.

The model results on various near-surface fields were compared with corresponding ship observations for the 1950–93 period, as assembled in the Comprehensive Ocean–Atmosphere Data Set (see Woodruff et al. 1987) and compiled by DaSilva et al. (1994).

3. North Pacific sea–air coupling associated with ENSO

a. Lagged regression patterns of the SST field versus ENSO

To depict the temporal evolution of the North Pacific SST field accompanying ENSO episodes in the tropical

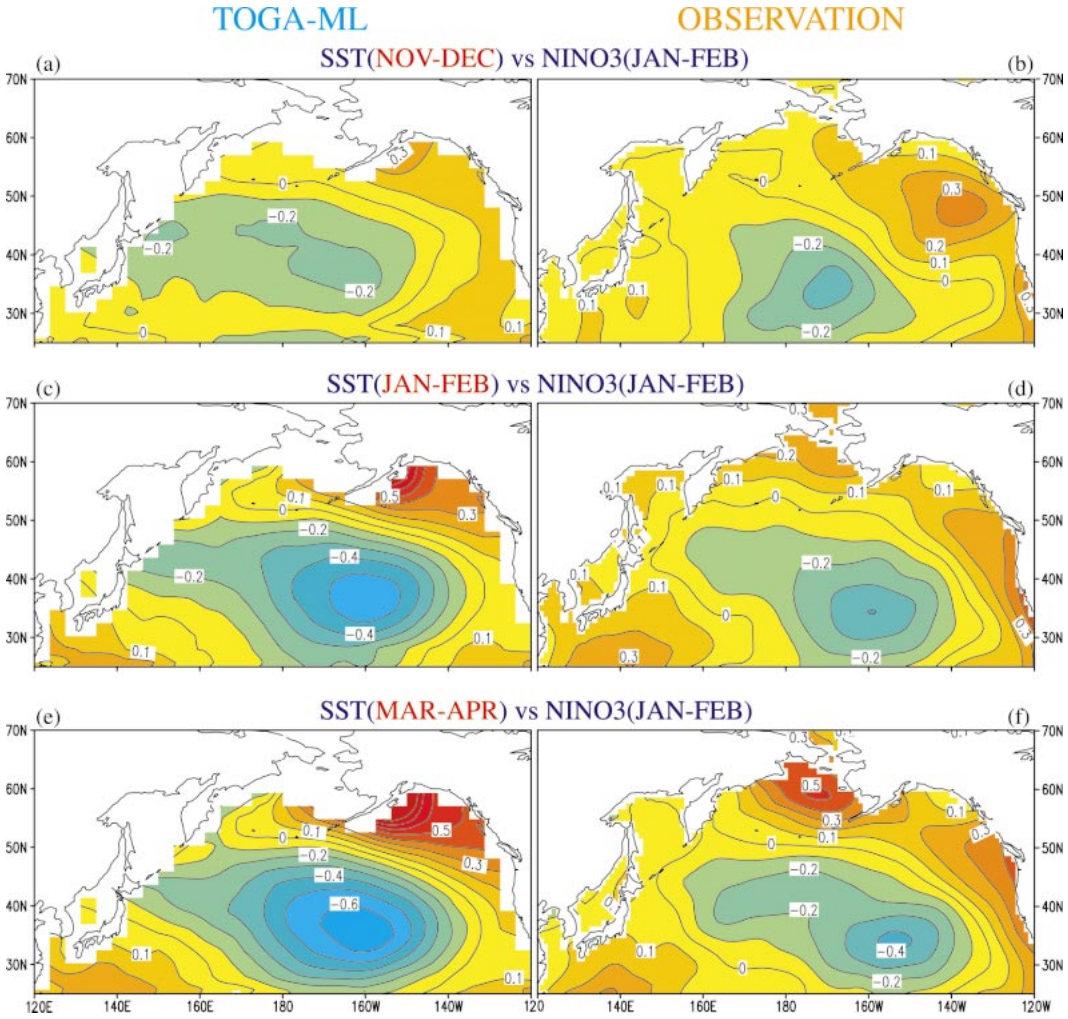

FIG. 1. Regression coefficients of bimonthly averages of SST (°C) in the North Pacific vs the standardized Niño-3 SST index for Jan–Feb. Results based on North Pacific data for (top) Nov–Dec (at a 2-month lead), (middle) Jan–Feb (simultaneous) and (bottom) Mar–Apr (at a 2-month lag). Left panels show patterns based on four-run ensemble averages of the SST field simulated in TOGA-ML. Right panels show the corresponding observations.

Pacific, a lagged regression analysis has been performed using the SST time series for individual extratropical grid points and the time series of an ENSO index. The latter indicator is chosen to be the observed SST averaged over the central and eastern equatorial Pacific (5°S–5°N, 90°–150°W), often referred to as the Niño-3 region. The left panels in Fig. 1 show the distributions of the regression coefficients using four-run ensemble means of the North Pacific SST simulated in the TOGA-ML experiment. The right panels show the corresponding results based on the observational SST dataset analyzed by DaSilva et al. (1994). The common ENSO index used in all computations presented here is the standardized, bimonthly averages of SST values in Niño-3 for January–February. The top panels depict the results obtained by regressing the bimonthly averages of North Pacific SST for November–December in a given year upon the ENSO index for January–February in the following year (i.e., with North Pacific SST *leading* the ENSO index by two months). The middle panels illustrate the patterns for zero lag between SST variations in the North Pacific and the Niño-3 region. The bottom panels show the results with North Pacific SST *lagging* the ENSO index by two months (i.e., extratropical SST for March–April versus the ENSO index). The regression data presented in various panels in Fig. 1 indicate the typical SST changes in the North Pacific for a positive SST anomaly of one standard deviation in the Niño-3 region.

Both the TOGA-ML and observational results presented in Fig. 1 reveal that warm SST anomalies in the tropical Pacific are accompanied by below-normal temperatures within the 35°–50°N zone in the central North Pacific, and above-normal temperatures off the western coast of North America and in the subtropical waters south of Japan. Cold events in the tropical Pacific would

be linked to North Pacific SST variations with polarities that are opposite to those portrayed in Fig. 1. The principal features in Fig. 1 have previously been documented in many observational studies (e.g., Namias and Cayan 1981; Wallace et al. 1990; Deser and Blackmon 1995). By comparing the amplitudes of the signals appearing in the top, middle, and bottom panels, it is evident that the North Pacific SST anomalies are much stronger when they lag the ENSO index (see Figs. 1e and 1f) than when they lead the same index (Figs. 1a and 1b). This notable asymmetry of the regression coefficients with respect to the temporal lag suggests that the SST pattern in Fig. 1 can be interpreted as a response to ENSO-related forcing in the tropical Pacific.

The model and observed patterns in Fig. 1 are in general agreement with each other. The negative SST anomaly in the observation (right panels) is confined to the central portion of the Pacific basin; whereas the same feature in the model result (left panels) extends more westward to the eastern Asian seaboard. The observed warm anomaly off the western U.S. coast is less evident in the model results, probably due to the absence in the TOGA-ML experiment of oceanic processes such as horizontal advection, upwelling, and coastally trapped waves. The magnitudes of the North Pacific SST changes at zero and two-month lags (middle and bottom panels) in the model simulation are larger than the corresponding observed values. A contributing factor to this discrepancy is the assumption of a constant 50-m depth for the mixed layer at all ocean grid points in the TOGA-ML experiment. Observational estimates (e.g., Levitus 1982) indicate that the mixed layer in extratropical oceans during winter and early spring is actually deeper than this assumed value. When subjected to atmospheric driving of a given strength, the comparatively larger thermal capacity of the observed mixed layer would lead to a weaker SST response than that simulated using the thinner 50-m slab. The stronger SST signals in the model patterns may also be partially attributed to the relatively large wind and heat flux anomalies simulated in TOGA-ML, as shown in sections 3b and 3c (see Figs. 3 and 4).

Lagged regression coefficients versus ENSO indices for calendar months other than January–February have also been computed. The results (not shown) generally indicate lower amplitudes and weaker temporal development than those presented in Fig. 1. Our choice of the January–February period for defining the ENSO index is further justified by the results to be presented later in this paper. These findings generally indicate a maximum atmospheric response to ENSO in January–February, followed by peaks in the SST signals 1–2 months later.

To illustrate the variability of the simulated SST signals among various outstanding warm and cold ENSO events in the 1950–95 period and among the four samples of the TOGA-ML experiment, spatial averages of the SST anomalies at selected sites have been computed for individual ENSO events and individual samples. The two sites chosen for this purpose are located in the subtropical central North Pacific (Site A) and Gulf of Alaska (Site B), and correspond to the principal anomaly centers in the regression patterns in Fig. 1. The boundaries of these sites are depicted in Fig. 3e. The eight warm ENSO episodes used in this composite procedure are those with central equatorial Pacific SST anomalies peaking toward the end of 1957, 1965, 1969, 1972, 1976, 1982, 1987, and 1991, or the beginning of the following year. The eight cold events are those attaining full amplitudes near the end of 1950, 1954, 1955, 1964, 1970, 1973, 1975, and 1988, or the beginning of the following year. These prominent episodes have been identified in many previous investigations (see review by Trenberth 1997). The years listed above are labeled as ''Year (0),'' and the years thereafter as ''Year (+1).'' A specific month in the temporal sequence of the composite anomalies is identified by that month followed by the year (0 or +1) in parentheses, for example, November (0) refers to November in Year (0), etc.

The areal-averaged SST anomalies in March–April (+1) for each of the warm and cold events and each of the four TOGA-ML integrations are displayed using open circles in Fig. 2, for Sites A (upper panels) and B (lower panels). The data values have been normalized by the standard deviation for the corresponding model run. The average of the standardized anomalies simulated in the four individual runs during a given ENSO event is indicated using a filled circle. Inspection of the data presented in Fig. 2 confirms that a majority of the TOGA-ML runs yield negative SST anomalies in Site A and positive anomalies in Site B during most of the warm events (left panels). The polarities of these simulated SST anomalies are reversed in most of the cold events (right panels). With very few exceptions, the four-run ensemble means (filled circles) share the same polarity in a given panel in Fig. 2.

b. Regression patterns of other surface fields versus ENSO

The myriad of processes contributing to the North Pacific SST anomaly pattern in Fig. 1 may be delineated by local changes in the atmospheric circulation and temperature fields near the ocean surface, and the resulting perturbations in the heat exchange at the sea–air interface during ENSO events. The regression patterns of selected surface fields versus the observed Niño-3 SST index are shown in Fig. 3. These fields include the near-surface horizontal wind vector (arrows) and wind speed (color shading) in the top panels, surface air temperature in the middle panels, and the sum of sensible and latent heat fluxes in the bottom panels. Results based on four-run ensemble averages for the TOGA-ML experiment are presented in the left panels. The corresponding patterns deduced from ship measurements as analyzed by DaSilva et al. (1994) are given in the right panels. All

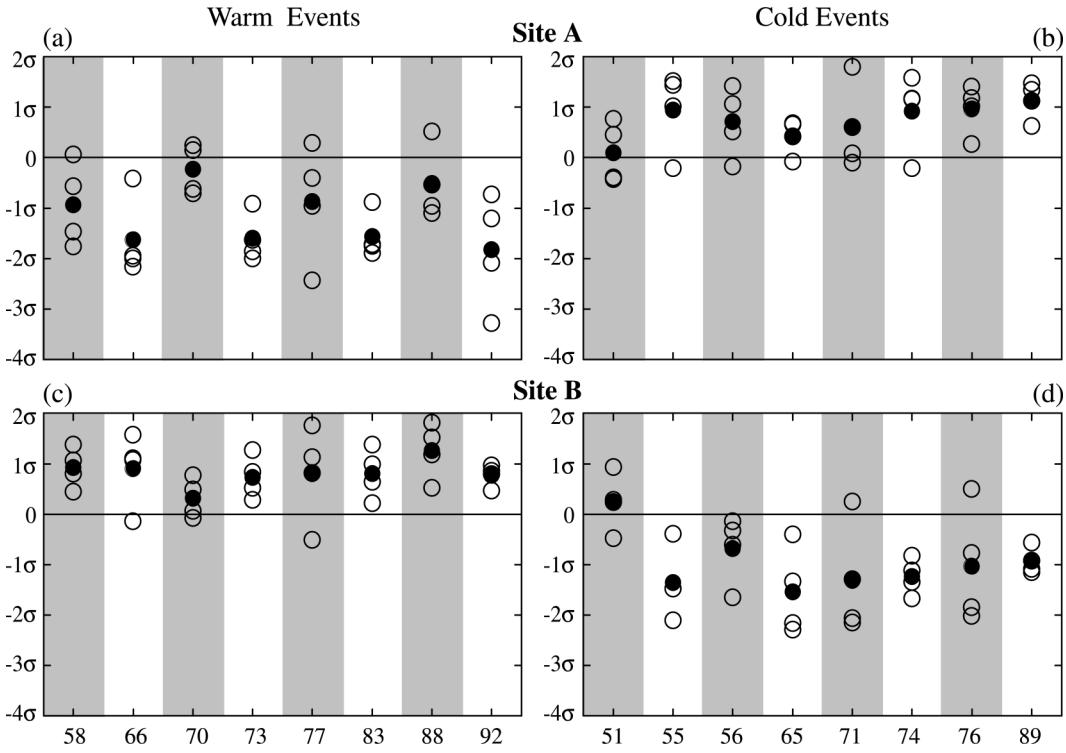

FIG. 2. Area-averaged SST anomalies for Mar–Apr (+1) in each of the eight selected (left) warm ENSO events and (right) cold events. Results for Sites A and B (see locations in Fig. 3e) are displayed in the top and bottom panels, respectively. Open circles indicate data for the four individual TOGA-ML runs, with the anomalies for each run being normalized by the standard deviation of the 46-yr time series for the respective run. Filled circles indicate the corresponding four-run averages.

computations have been performed using bimonthly averages of both surface fields and the Niño-3 SST index for January–February, during which the northern extratropical teleconnections with ENSO are most evident (e.g., see Trenberth et al. 1998). The sign convention for the surface fluxes in Figs. 3e and 3f is such that positive (negative) flux anomalies lead to warming (cooling) of the oceanic mixed layer.

The top panels of Fig. 3 indicate that warm ENSO events are coincident with a cyclonic atmospheric circulation anomaly near the surface of the North Pacific. The westerly anomalies on the southern flank of this cyclonic feature strengthen the eastward climatological flow in that region, thus increasing the local wind speed (see red shading along the 30°–45°N belt in Figs. 3a and 3b). The enhanced northwesterly flow situated west and southwest of the cyclonic center is accompanied by below-normal air temperature near the surface (Figs. 3c and 3d). Conversely, warm temperatures prevail off the west coast of North America, where the anomalous circulation is directed poleward. Regression charts for near-surface water vapor mixing ratio (not shown) are qualitatively similar to those for air temperature, with dry anomalies being collocated with cold temperatures, and vice versa.

The sensible and latent heat fluxes across the sea–air interface are computed in the GCM using the bulk aerodynamic law, which assumes that these fluxes are proportional to the product of the wind speed and sea–air differences in temperature and water vapor mixing ratio (see details in section 3c). The regression patterns for the sum of sensible and latent heat fluxes (Figs. 3e and 3f) are seen to be consistent with the wind and temperature anomalies discussed above. Specifically, the stronger wind speeds south of the anomalous cyclone as well as the advection of cold and dry air masses to the western and central portions of the North Pacific enhance the heat loss from the ocean in those regions (thus leading to cooling of the mixed layer); whereas warm and moist advections along the eastern and northeastern sectors of the cyclonic anomaly reduce oceanic heat loss. Comparison between the left and right panels of Fig. 3 indicates that some correspondence exists between the simulated surface fields and their observational counterparts. The wind and temperature anomalies based on model data have relatively higher amplitudes. The principal features in Fig. 3 also resemble the observed wind and surface flux anomalies associated with leading modes of SST or sea level pressure variability in the North Pacific, as documented by Cayan (1992a, their Fig. 4) and Deser and Blackmon (1995, their Fig. 4a).

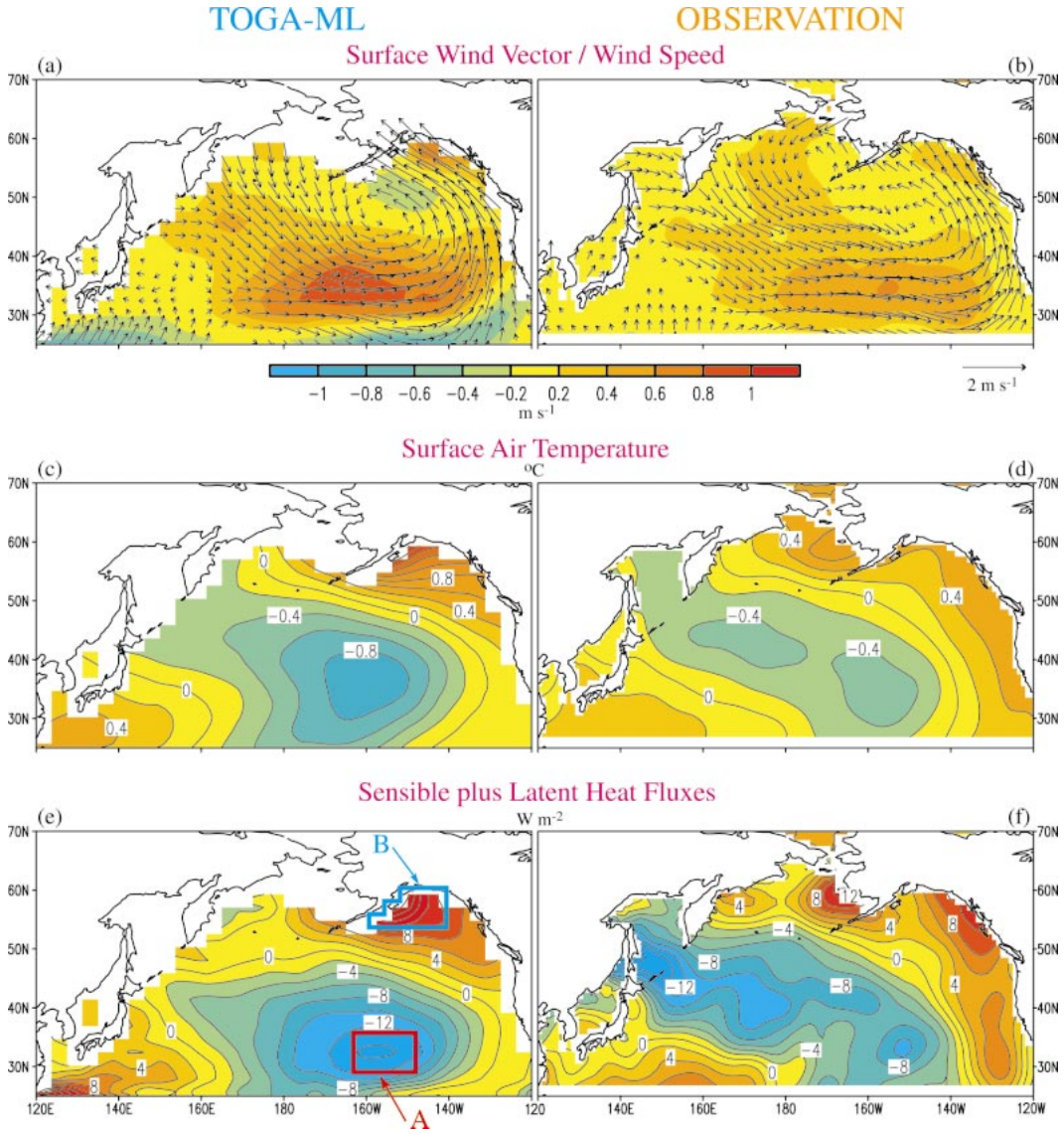

FIG. 3. Simultaneous regression coefficients of various near-surface quantities in the North Pacific vs the standardized Niño-3 SST index for Jan–Feb: (top) surface wind vector [arrows, see scale at bottom right of (b)] and wind speed (shading, see scale bar); (middle) surface air temperature (contour interval: 0.2°C); (bottom) sensible plus latent heat fluxes (contour interval: 2 W m^{-2}; defined to be positive when these fluxes lead to warming of oceanic mixed layer). Left panels show patterns based on four-run ensemble averages simulated in TOGA-ML. Right panels show the corresponding observations. Indicated in (e) are the boundaries of Sites A and B, for which area-averaged quantities are displayed in Figs. 4 and 5.

The salient similarities between the patterns for heat fluxes (Figs. 3e and 3f) with those for SST (Fig. 1) suggest that the surface fluxes play a significant role in the formation of SST perturbations in the North Pacific during ENSO episodes. This finding is in accord with that of Cayan (1992b), who reported strong temporal and spatial correlations between observed anomalies in heat flux and SST tendency over the extratropical oceans. However, the results of Miller et al. (1994) and Seager et al. (2000) indicate that the SST conditions may also be influenced by other processes in the ocean interior, such as Ekman transport and vertical mixing.

c. *Surface heat budget*

We proceed to examine the detailed seasonal evolution of the surface variables in selected sites, and the effects of seasonality on the local surface heat budget. The sensible and latent heat fluxes (F_S, F_L, respectively) can be written as $F_S = -C_S V(T_o - T_a)$ and $F_L = -C_L V(q_o - q_a)$, where $C_S = \rho C_p C_d$, $C_L = \rho L C_d$, ρ is the air density, C_p is the specific heat of air at constant pressure, L is the latent heat of evaporation, C_d is the drag coefficient, V is the surface wind speed, T is the surface temperature, q is the surface water vapor mixing

ratio, the subscripts o and a refer to the ocean and atmosphere, respectively, and q_o is the saturation mixing ratio at T_o. Using linearization, perturbations in these fluxes may be approximated as

$$F'_S \approx -C_S[V'(\overline{T_o} - \overline{T_a}) + \overline{V}(T'_o - T'_a)], \quad (1)$$

$$F'_L \approx -C_L[V'(\overline{q_o} - \overline{q_a}) + \overline{V}(q'_o - q'_a)], \quad (2)$$

where the overbar and prime represent time averages and deviations from time averages, respectively. In deriving the above expressions, contributions from temporal covariances between V' and the quantities T'_o, T'_a, q'_o, and q'_a have been neglected. The contributions of the products between the time-mean and fluctuating quantities to F'_S and F'_L may hence be discerned by considering the temporal development of the climatological and anomalous components of V and sea–air differences in T and q. Analogous diagnoses of various components of the surface heat fluxes have previously been performed by Cayan (1992a), Alexander and Scott (1997), and Enfield and Mayer (1997).

In Figs. 4 and 5 are shown the month-to-month variations of the long-term averages of T_a, T_o, q_a, q_o, and V (upper three panels); the anomalies of the same quantities (middle three panels); and the anomalies of various components of the surface heat budget (bottom panel). All anomalies are computed by subtracting the composite of the four-run means over eight outstanding cold ENSO events in the 1950–95 period from the composite over eight warm events in the same period. We shall henceforth refer to these anomalies as the ''warm minus cold composites.'' The warm and cold ENSO episodes used in this composite procedure have been listed in section 3a (see also Fig. 2). Individual contributions to the anomalous fluxes at the sea–air boundary are depicted in the bottom panel of Figs. 4–5 using a cumulative format. In order to focus our attention on the effects of the interplay between wind speed and sea–air gradients, both the observed and simulated heat fluxes have been estimated by setting C_d to the constant value used in the GCM integrations (i.e., 1×10^{-3}), and by using climatological values of ρ. The results presented here are areal averages over Sites A (Fig. 4) and B (Fig. 5), which correspond to the two principal centers of SST and heat flux variability in the North Pacific (see boundaries depicted in Fig. 3e).

1) SITE A

Data for Site A from the TOGA-ML experiment and the observational data compiled by DaSilva et al. (1994) are displayed in the left and right halves of Fig. 4, respectively. The observational results presented in this figure are based on ship measurements in individual grid boxes. No spatial interpolation or analysis have been applied to the latter grid values. The following discussion mostly pertains to the model results. Comparison between model and observational data will be made below. The model climatology is characterized by positive $\Delta\overline{T} = \overline{T}_o - \overline{T}_a$ and $\Delta\overline{q} = \overline{q}_o - \overline{q}_a$ throughout the November–May period (see Figs. 4a and 4b). In accord with the regression results in Figs. 3a and 3b, the warm minus cold composites of V' in Fig. 4f show increased wind speeds at this site, with maximum amplitudes in January–February (+1). The action of anomalous wind speeds on the climatological sea–air differences (through the terms $-C_S V'\Delta\overline{T}$ and $-C_L V'\Delta\overline{q}$) leads to cooling of the oceanic mixed layer, with maximum contributions to the surface heat budget occuring in January–February (+1) (see Fig. 4g).

The climatological surface wind speeds $\overline{V}$ are highest in January–February (Fig. 4c). The warm minus cold composites of T and q (Figs. 4d and 4e) indicate that the predominately negative anomalies of T'_a and q'_a attain maximum strength in January–February (+1). The corresponding variations of T'_o and q'_o exhibit a temporal lag of 1–2 months behind those of T'_a and q'_a, with the largest oceanic anomalies typically occurring in February–March (+1). This lag relationship is accompanied by positive values $\Delta T' = T'_o - T'_a$ and $\Delta q' = q'_o - q'_a$ in December (0)–February (+1). The action of the climatological flow on these anomalous sea–air gradients (through the $-C_S\overline{V}\Delta T'$ and $-C_L\overline{V}\Delta q'$ terms) results in oceanic cooling and further enhancement of the concomitant negative T'_o anomaly at this site (see Fig. 4g). The amplitudes of T'_a and q'_a are seen to decrease noticeably in the spring of Year (+1); whereas the attenuation of the signals in T'_o and q'_o is delayed and more moderate. In Figs. 4d and 4e, the curves for the atmospheric (blue) and oceanic (red) variables typically cross each other between February and March (+1). In the months following this crossover, the polarity of $\Delta T'$ and $\Delta q'$ is reversed, the terms $-C_S\overline{V}\Delta T'$ and $-C_L\overline{V}\Delta q'$ become positive and act to diminish the cold SST anomaly in Site A (Fig. 4g). The contributions of shortwave and longwave radiative fluxes to the surface heat budget in the TOGA-ML experiment (not shown) are generally smaller than those of anomalous sensible and latent heat fluxes presented in Fig. 4g.

The seasonal evolution of the anomalous heat fluxes during warm ENSO events in the TOGA-ML experiment may be summarized as follows: both the products of V' with $\Delta\overline{T}$ and $\Delta\overline{q}$, and the products of $\overline{V}$ with $\Delta T'$ and $\Delta q'$, result in cooling of the oceanic mixed layer from November (0) through February–March (+1). In the following spring, V' drops to near zero and the contributions of $-C_L V'\Delta\overline{q}$ and $-C_S V'\Delta\overline{T}$ are markedly reduced. Concurrently, $\Delta T'$ and $\Delta q'$ switch polarity, $\overline{V}$ remains large as compared with V', so that $-C_S\overline{V}\Delta T'$ and $-C_L\overline{V}\Delta q'$ become positive and act to oppose the cold anomaly of the mixed layer.

Qualitative agreement exists between the model and observational results in Fig. 4. Both the observed and simulated variations of T'_a, T'_o, q'_a, and q'_o in Figs. 4d and 4e indicate the intersection between the red and blue curves in February–March (+1), as mentioned ear-

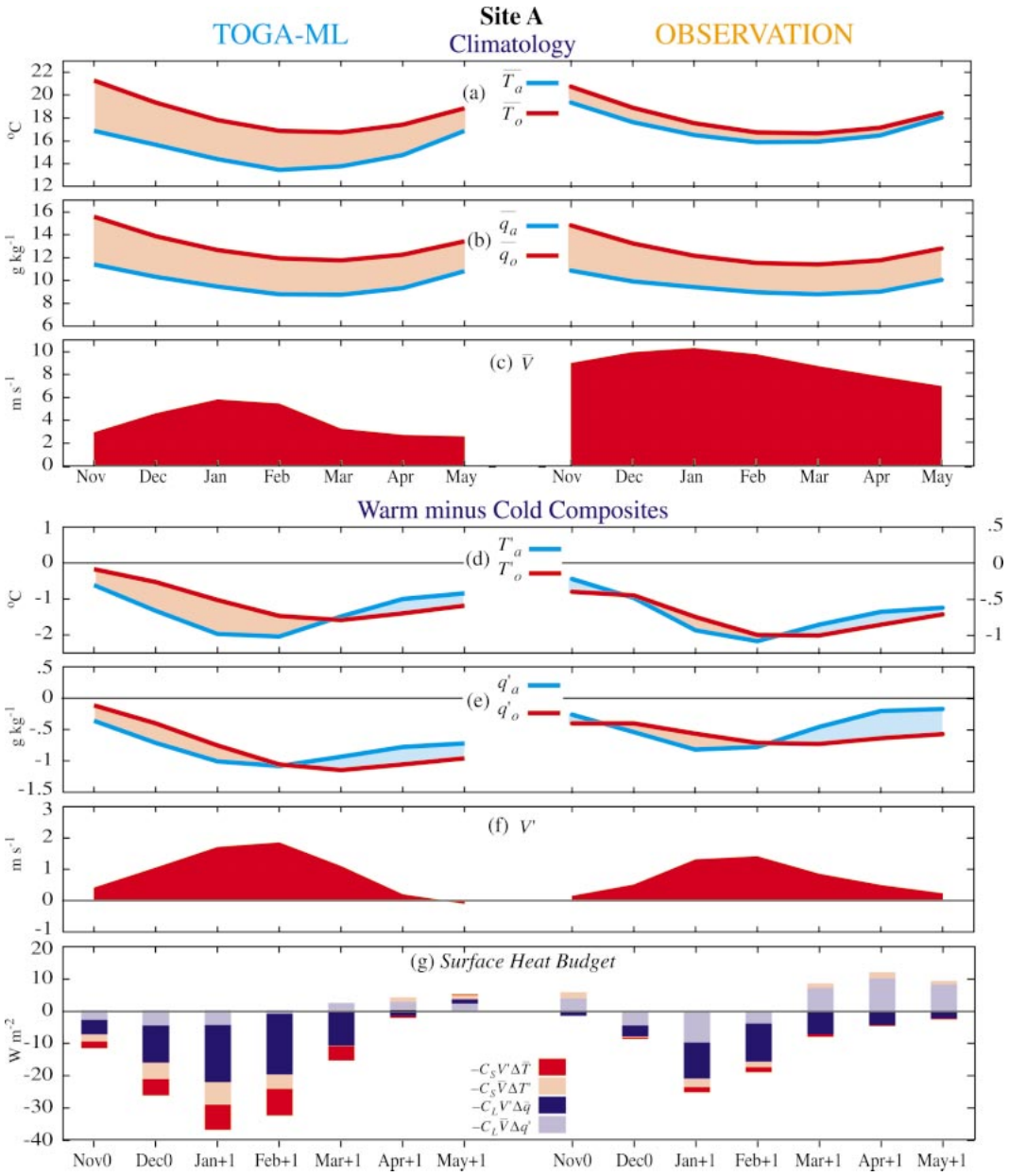

FIG. 4. Temporal variations of different area-averaged quantities for Site A (see location in Fig. 3e). Results are shown for the climatologies from Nov to May of (a) surface air temperature (T_a) and ocean temperature (T_o), (b) surface water vapor mixing ratio (q_a) and saturation mixing ratio at T_o (q_o), and (c) surface wind speed (V) and for warm minus cold composites from Nov (0) to May (+1) of (d) T_a and T_o, (e) q_a and q_o, and (f) V. Warm minus cold composites of various components of the surface heat fluxes (defined to be positive when these fluxes lead to warming of the oceanic mixed layer) from Nov (0) to May (+1) are shown in (g). Results based on four-run ensemble averages simulated in TOGA-ML are presented in the left half of each panel. The corresponding observations are displayed in the right half. The scaling of the ordinate axes for the model data is the same as that for observational data, except in (d). Light red (light blue) stippling in (a), (b), (d), and (e) indicate positive (negative) sea–air gradients $T_o - T_a$ or $q_o - q_a$.

lier in this section. The amplitudes of the observed T'_a and T'_o are smaller than those in the model experiment (note different scales used in plotting the two halves of Fig. 4d). The $-C_L\overline{V}\Delta q'$ term is seen to play a more prominent role in the observed heat budget than in the model budget, primarily due to the notably higher values of the observed $\overline{V}$ (see Fig. 4c). The smaller magnitudes of the observed sensible heat flux terms as compared to the model values can be attributed to the weaker $\Delta\overline{T}$ and $\Delta T'$ (see Figs. 4a and 4d) based on ship measurements.

To test the accuracy of the linearized form of F'_S and

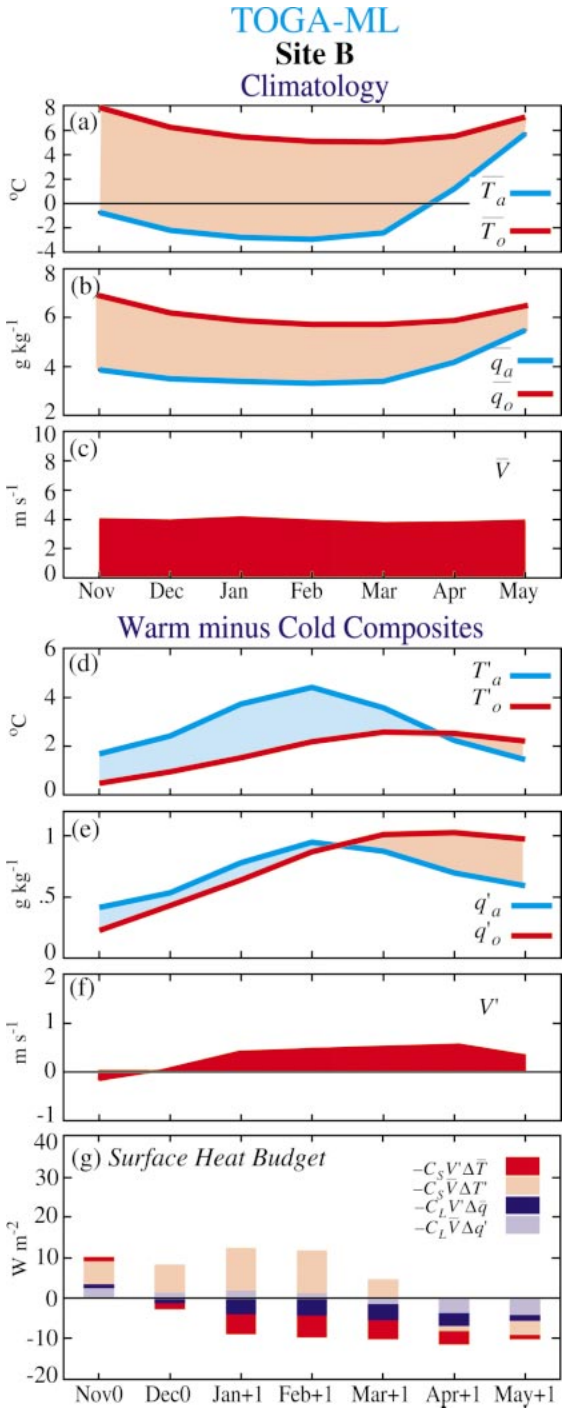

FIG. 5. As in Fig. 4, but for Site B (see location in Fig. 3e) and for TOGA-ML data only.

F'_L [see Eqs. (1) and (2)], warm minus cold composites have also been constructed using the actual sensible and latent heat fluxes from the model archives. These fluxes have been computed on a daily basis using the instantaneous values of V, ΔT, and Δq in the course of the TOGA-ML experiment. Composites of the flux data include contributions from the linear terms in Eqs. (1) and (2) as well as nonlinear effects due to temporal covariances between V' and $\Delta T'$ or $\Delta q'$. The composite values of the actual fluxes for Site A (not shown) are generally within ~20% of the estimates based on Eqs. (1) and (2) during the midwinter months, thus indicating that the nonlinear terms are of secondary importance for this site.

2) SITE B

Results of the budget analysis based on model data for Site B are presented in Fig. 5. In analogy to the situation in Site A, the atmospheric temperature anomalies lead the SST anomalies, with the former peaking in February (+1) and the latter in March–April (+1) (Fig. 5d). The curves for T'_a and T'_o intersect each other in March–April (+1), so that $\Delta T'$ is negative prior to this crossover point, and positive thereafter.

Because of the weak amplitudes of V', contributions of the terms $-C_S V'\Delta\overline{T}$ and $-C_L V'\Delta\overline{q}$ at Site B (see Fig. 5g) are smaller than those at Site A (Fig. 4g). The magnitude of $\Delta T'$ at Site B (Fig. 5d) is larger than that at Site A (Fig. 4d; note different scales used), so that $-C_S\overline{V}\Delta T'$ becomes a dominant term in the heat budget during winter months (Fig. 5g). These contrasts in the relative importance of various components in the heat budgets at Sites A and B are consistent with the findings of Cayan (1992a) and Seager et al. (2000), who noted that heat flux anomalies at open maritime sites (such as A) are primarily due to wind variability (i.e., V'), whereas atmospheric advection of T and q exert strong influences on the fluxes near coastal regions (such as B).

4. North Atlantic sea–air coupling associated with ENSO

We now turn our attention to ENSO-related fluctuations in the atmosphere–ocean system in the North Atlantic. Regression and budget analyses analogous to those presented in the previous section are repeated here for the North Atlantic domain. Physical considerations similar to those applied to the North Pacific will be used to interpret the following results.

a. Regression patterns

The distributions of the regression coefficients of SST at individual grid points in the North Atlantic versus the Niño-3 SST index in January–February are displayed in Fig. 6, for Niño-3 lagging North Atlantic by two months (top panels), zero lag (middle panels), and Niño-3 leading North Atlantic by two months (bottom panels). Model (observational) results are shown in the left (right) panels. In view of the weaker SST changes in the North Atlantic as compared with those in the North Pacific, the contour interval used in Fig. 6 is one-half of that in Fig. 1. Inspection of these patterns from

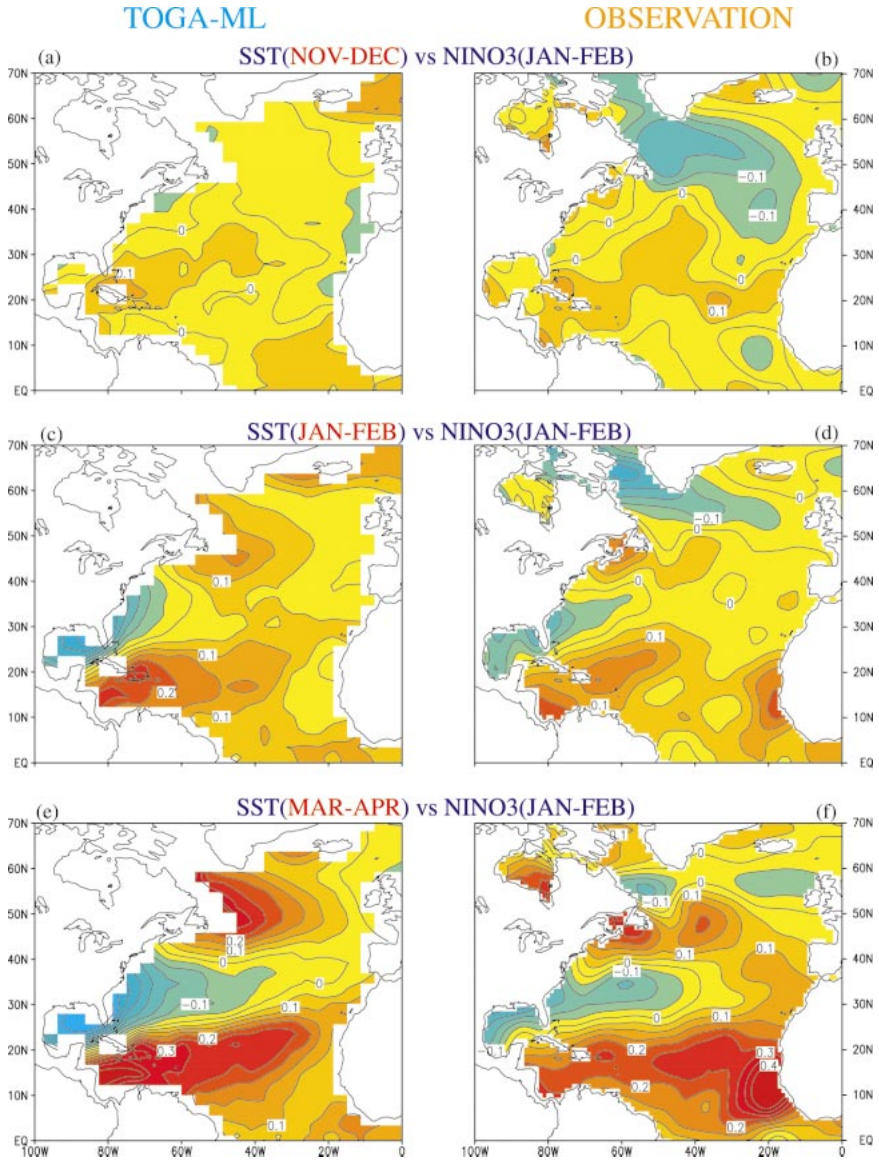

FIG. 6. As in Fig. 1, but for the North Atlantic. Contour interval is one-half that of Fig. 1.

top to bottom reveals the emergence of a tripolar signal from late fall to early spring, with warm ENSO events being associated with above-normal SST along two zonally elongated belts centered at ~15° and ~50°N, and with below-normal temperature in the waters extending from the Gulf of Mexico to the eastern U.S. seaboard. This characteristic pattern is similar to that reported in previous observational studies (e.g., Wallace et al. 1990; Deser and Blackmon 1993). The emergence of the warm anomaly in the subtropical North Atlantic from winter to spring during warm ENSO events is also evident in the observational data presented by Curtis and Hastenrath (1995, see their Fig. 2). The amplitudes of the SST changes are distinctly higher when the Niño-3 index leads the North Atlantic (Figs. 6e and 6f) than when Niño-3 lags the North Atlantic (Figs. 6a and 6b). These results imply that the impact of ENSO is not confined to the Pacific basin, but also extends to the Atlantic sector.

The broad-scale patterns based on model data are similar to the observations, especially when Niño-3 leads the North Atlantic (Figs. 6e and 6f). The simulated features exhibit a stronger spatial coherence than those appearing in the observed patterns. There is no indication in the model result of the negative SST changes observed along a narrow band centered at ~55°N. In early spring, the strongest warm SST anomalies within the belt south of 25°N are observed off the African coast, whereas the maximum in the simulated pattern is located in the Caribbean Sea. The observed SST feature near Africa could in part result from reduced coastal upwelling due to the weakened northeasterly trades in that

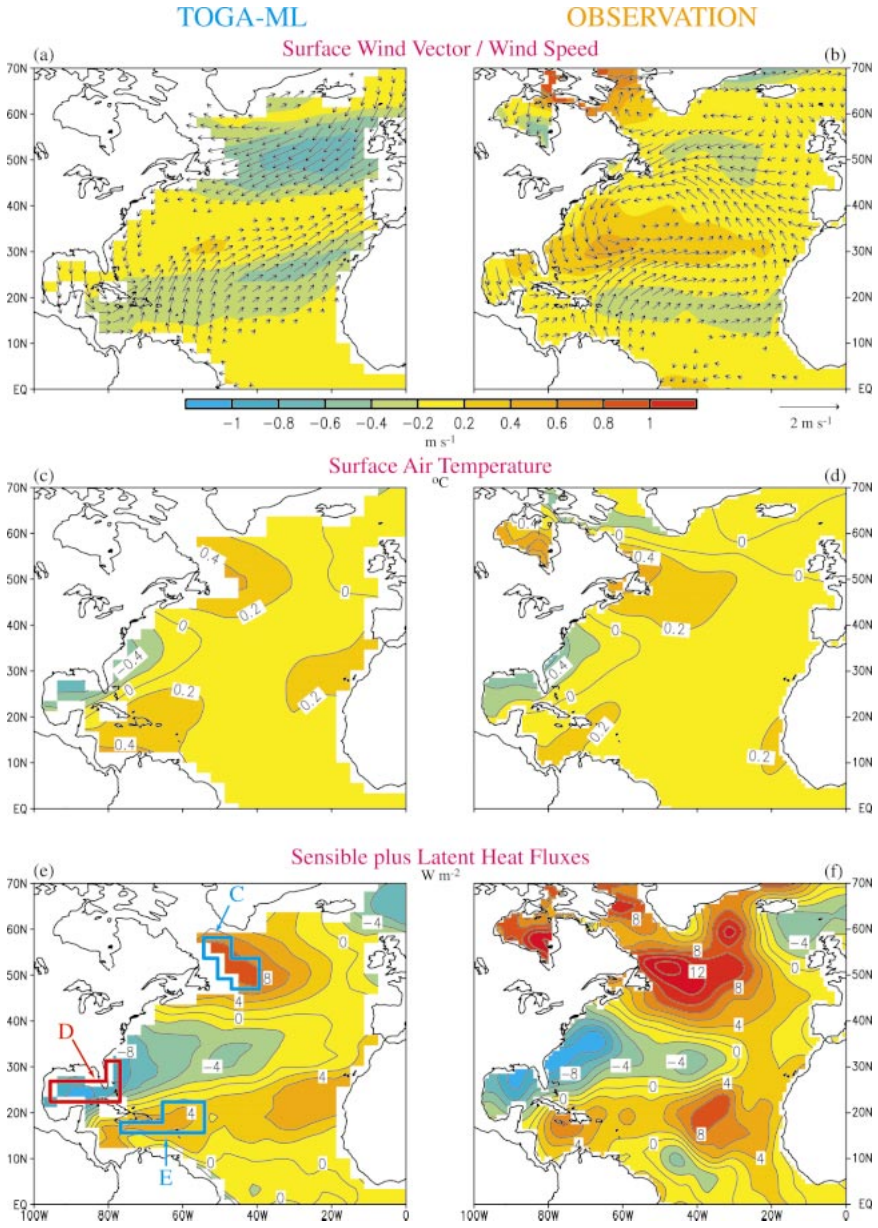

FIG. 7. As in Fig. 3, but for the North Atlantic. Indicated in (e) are the boundaries of Sites C, D, and E, for which area-averaged quantities are displayed in Fig. 8.

region during warm ENSO events (see Fig. 7b to be presented in the following paragraph). This feature is absent in the model pattern, since the upwelling mechanism has not been incorporated in the TOGA-ML experiment.

The simultaneous regression charts of surface wind vector and wind speed, air temperature, and sum of sensible and latent heat fluxes in January–February are presented in Fig. 7 for both model and observational data. Warm ENSO events are seen to coincide with an anomalous North Atlantic surface anticyclone with axis at ~60°N, and an anomalous cyclone centered at ~35°–40°N (Figs. 7a and 7b). The easterly flow anomalies south of the anticyclonic center oppose the local climatological westerlies, thus leading to below-normal wind speeds in that region. The band of westerly anomalies south of the cyclonic feature spans the zone of climatological westerlies situated north of ~25°N and the easterly trade wind belt south of that latitude. Consequently, the wind speeds in the zone of prevalent westerlies are enhanced, whereas the strength of the trades is reduced. Advection of warm maritime air masses by the easterly anomalies along the 40°–60°N belt results in above-normal air temperatures off the eastern Canadian coasts (Figs. 7c and 7d). Negative temperature anomalies are seen off the eastern U.S. seaboard and

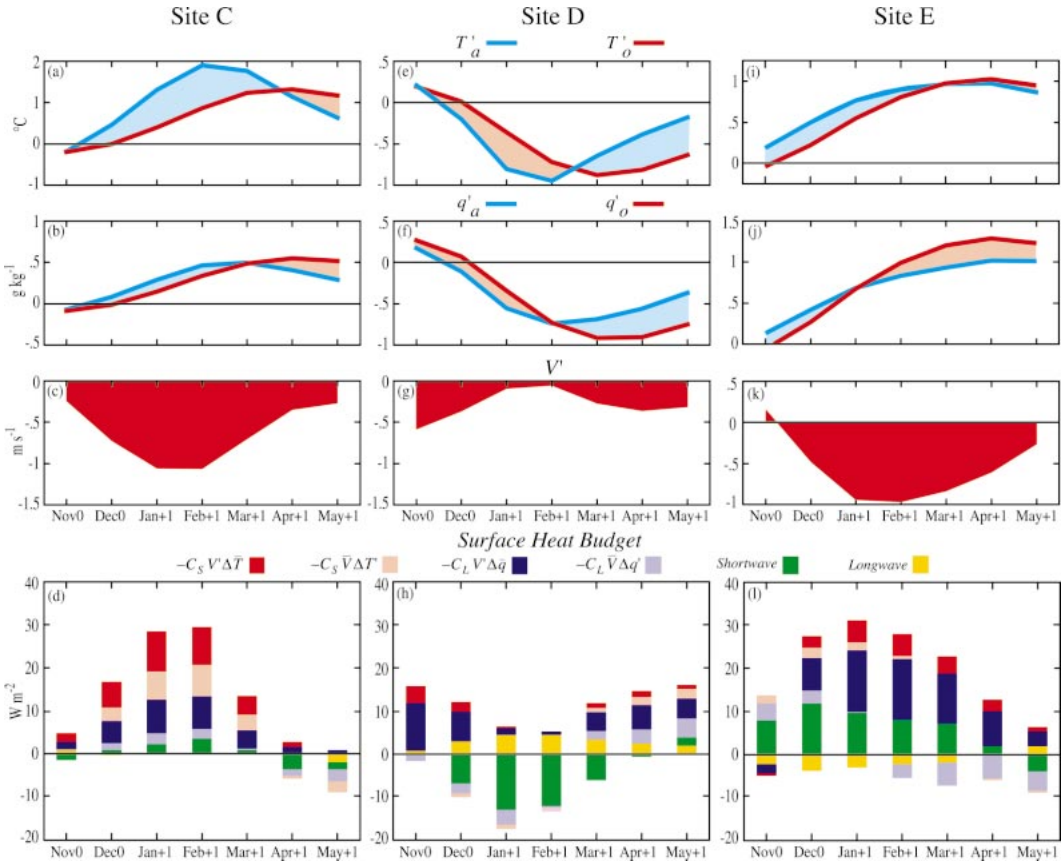

FIG. 8. As in Figs. 4 and 5, but for the North Atlantic Sites C (left), D (middle), and E (right), and for warm minus cold composites of the TOGA-ML data only.

over the Gulf of Mexico, which are under the influence of cold northerly winds from the North American landmass. Southerly winds off South America are accompanied by positive temperature anomalies in the Caribbean region. The decreased wind speeds and above-normal air temperatures in the 40°–60°N and 10°–25°N belts reduce the oceanic loss to the atmosphere through sensible and latent heat fluxes, and lead to warming of the mixed layer (Figs. 7e and 7f). On the other hand, increased wind speeds and below-normal air temperatures off the Atlantic and Gulf coasts of the United States are conductive to oceanic cooling. The midlatitude wind and flux patterns in Fig. 7 compare well with the observational results presented previously by Cayan (1992a) and Deser and Blackmon (1993). The subtropical features in Fig. 7 are consistent with the corresponding results documented by Curtis and Hastenrath (1995), Enfield and Mayer (1997), and Klein et al. (1999) based on observational data.

b. Surface heat budget

To evaluate the contributions of individual processes to the SST changes at various North Atlantic sites, the seasonal dependence of different components of the anomalous local surface fluxes has been analyzed using TOGA-ML data. These computations are analogous to those performed for the North Pacific sites (Figs. 4 and 5). The three Atlantic sites (C, D, and E) chosen for this investigation are indicated in Fig. 7e. They correspond to locations with the strongest heat flux and SST anomalies. The warm minus cold composites of T'_a, T'_o, q'_a, q'_o, V', and individual components of the surface fluxes at the Atlantic sites are presented in Fig. 8. Similar to the situation at Sites A and B (see Figs. 4a–c, 5a–c), the seasonal climatologies for $\overline{T}_a$, $\overline{T}_o$, $\overline{q}_a$, and $\overline{q}_o$ at the Atlantic sites (not shown) are characterized by positive values of $\Delta\overline{T}$ and $\Delta\overline{q}$ in the November–May period.

The negative wind speed anomalies at Sites C and E (Figs. 8c and 8k) account for the positive contributions to the surface fluxes through the $-C_S V'\Delta\overline{T}$ and $-C_L V'\Delta\overline{q}$ terms at these locations (Figs. 8d and 8l). In analogy to the results for the Pacific sites, the oceanic anomalies T'_o, q'_o at Sites C and D typically lag the atmospheric anomalies T'_a, q'_a by 1–2 months, with the blue and red curves in Figs. 8a, 8b, 8e, and 8f intersecting each other in late winter or early spring. These temporal relationships lead to $-C_S\overline{V}\Delta T'$ and $-C_L\overline{V}\Delta q'$ contributions with the same (opposite) polarity as T'_o in

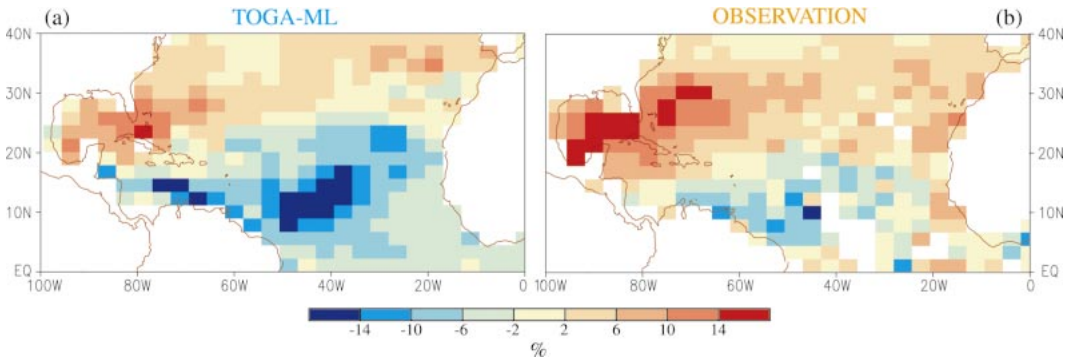

FIG. 9. Warm minus cold composites of the cloud amount at individual grid boxes (%; see scale bar at bottom) in Jan–Feb (+1), as computed using (a) TOGA-ML data and (b) ship observations. No color shading is used in grid boxes in (b) that have inadequate data coverage.

the period before (after) the intersection point (Figs. 8d and 8h).

The surface budget at Site C is dominated by the sensible and latent heat flux components (Fig. 8d). The contributions of shortwave radiative fluxes are more evident in Sites D and E (Figs. 8h and 8l). Changes in the shortwave fluxes in these regions are evidently related to anomalies in the cloud cover, as illustrated in Fig. 9, which shows the warm minus cold composites of the total cloud amount based on January–February (+1) data from (a) the TOGA-ML experiment and (b) the atlas compiled by DaSilva et al. (1994). The stronger northerly flow from the cold continent to the maritime zone near Site D (Figs. 7a and 7b) results in more cloud formation, thereby reducing the amount of incident solar radiation and cooling the surface ocean (Fig. 8h). The enhanced subsidence over the Caribbean Sea and subtropical Atlantic south of ~25°N during warm ENSO events (e.g., see Klein et al. 1999) is accompanied by decreased cloudiness (Fig. 9) and increased solar heating of the mixed layer (Fig. 8l). The composite cloud pattern based on ship observations (Fig. 9b) lends some support to the corresponding model result (Fig. 9a), especially in the western half of the basin. Some differences between model and observations are discernible near the African coast. Curtis and Hastenrath (1995) and Klein et al. (1999) have similarly documented the changes in cloud amount and radiative fluxes in the tropical Atlantic during ENSO events. Their findings also indicate that warm events are coincident with enhanced cloud cover north of 20°N, and reduced cloud amounts south of this latitude.

5. Ocean–atmosphere feedbacks in the extratropics

It is evident from the results presented in the previous two sections that the ENSO-related SST changes observed in the North Pacific and North Atlantic are primarily responses to anomalous atmospheric driving. The extratropical SST anomalies generated by this atmospheric bridge mechanism could in turn influence the overlying atmospheric conditions. The nature of such midlatitude sea–air feedbacks is the subject of investigation in the present section.

a. TOGA-ML versus TOGA: Dependence on location, season, and ENSO polarity

We first evaluate the impact on the atmosphere of the extratropical SST anomalies appearing in ENSO episodes. This issue is approached here by comparing the atmospheric signals in the TOGA-ML experiment with those in the TOGA experiment. Since the TOGA-ML experiment includes prescribed SST forcing in the tropical Pacific as well as simplified two-way sea–air interaction at ocean grid points elsewhere, the extratropical atmospheric signals in this simulation are the net result of both remote ENSO forcing and local ocean–atmosphere feedbacks.[1] On the other hand, the model atmosphere in the TOGA experiment is subjected exclusively to interannual SST changes within the tropical Pacific. Therefore the atmospheric responses in that experiment could be attributed to remote ENSO forcing only. Hence, to the first approximation, the influences of extratropical sea–air coupling on the local atmospheric variability may be inferred from the *differences* between the TOGA-ML and TOGA results.

The composites of the 500-mb-height anomalies over the eight selected warm ENSO events are shown in Fig. 10. Results for the TOGA-ML and TOGA experiments

[1] It is possible that SST anomalies generated in the tropical Indian and Atlantic Oceans in the TOGA-ML experiment (through tropical atmospheric bridges, e.g., see Enfield and Mayer 1997 and Klein et al. 1999) could in turn force teleconnection patterns in the extratropics. Such effects require further study by performing additional model runs with an experimental design similar to that of TOGA-ML, but with prescribed climatological SST conditions in the tropical Indian and Atlantic Oceans. Comparison of the output from such runs with the TOGA-ML results would reveal the contributions from SST variability in tropical oceans outside of the Pacific. This issue could also be addressed by prescribing SST forcing in the tropical Indian and Atlantic Oceans only, and analyzing the atmospheric responses in anomalous SST episodes occurring in those regions.

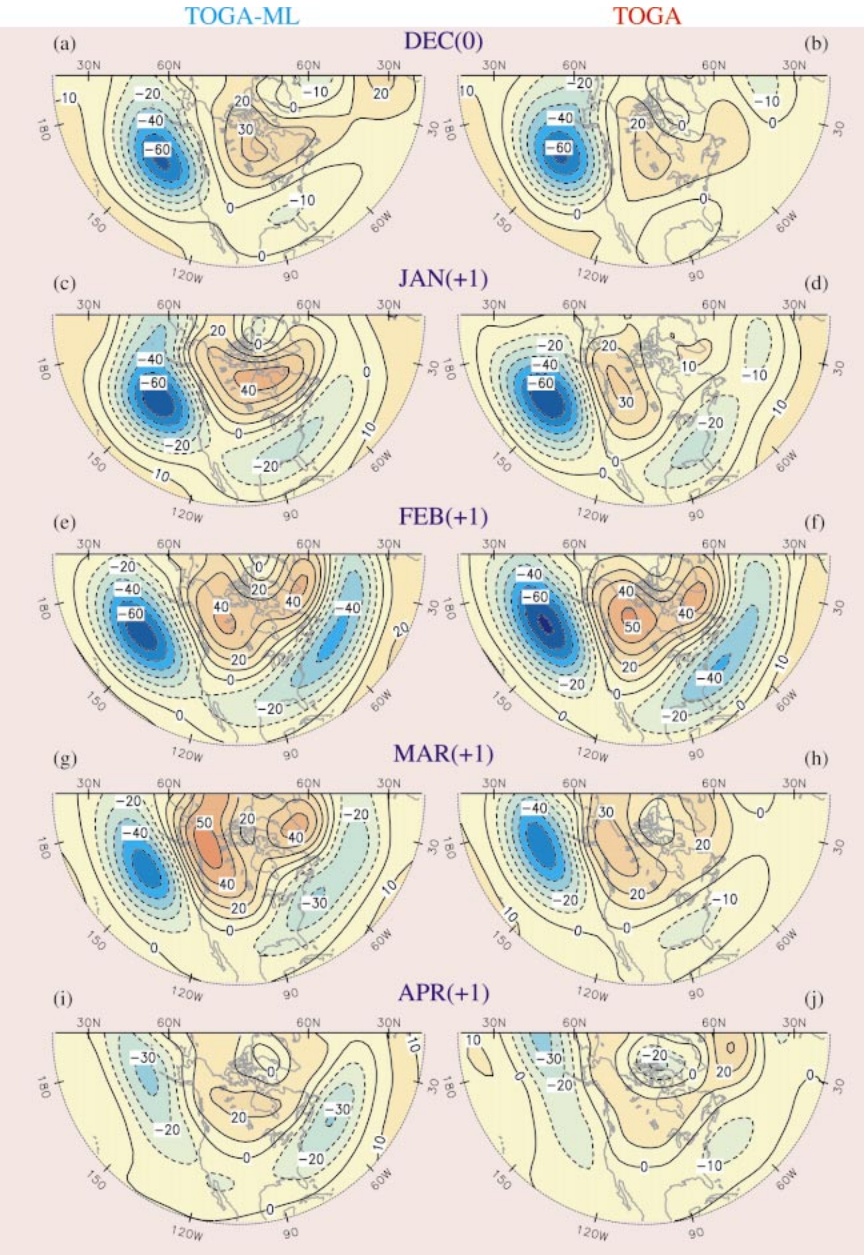

FIG. 10. Composites of 500-mb geopotential height anomalies (contour interval: 10 m) over eight warm ENSO events. Results are shown for individual months in the Dec (0)–Apr (+1) period. Patterns based on four-run ensemble averages of TOGA-ML and TOGA data are displayed in the left and right panels, respectively.

are displayed in the left and right halves of the figure, respectively. To depict the detailed evolution of the circulation anomalies, patterns are presented for each of the five calendar months in the December (0)–April (+1) period. The corresponding composites over the eight cold events are shown in Fig. 11. The model results in Figs. 10–11 have been compared with the corresponding observations (not shown) based on reanalysis data produced by the National Centers for Environmental Prediction and National Center for Atmospheric Research. It is seen that the TOGA-ML and TOGA experiments reproduce the observed teleconnection pattern associated with ENSO events. In particular, the warm composites for both model and observations are characterized by below-normal heights over the central North Pacific and the regions extending northeastward from the U.S. Gulf Coast to the western North Atlantic, and by above-normal heights over western Canada and Alaska. The polarities of these anomaly centers are reversed during cold events. The amplitude of the simu-

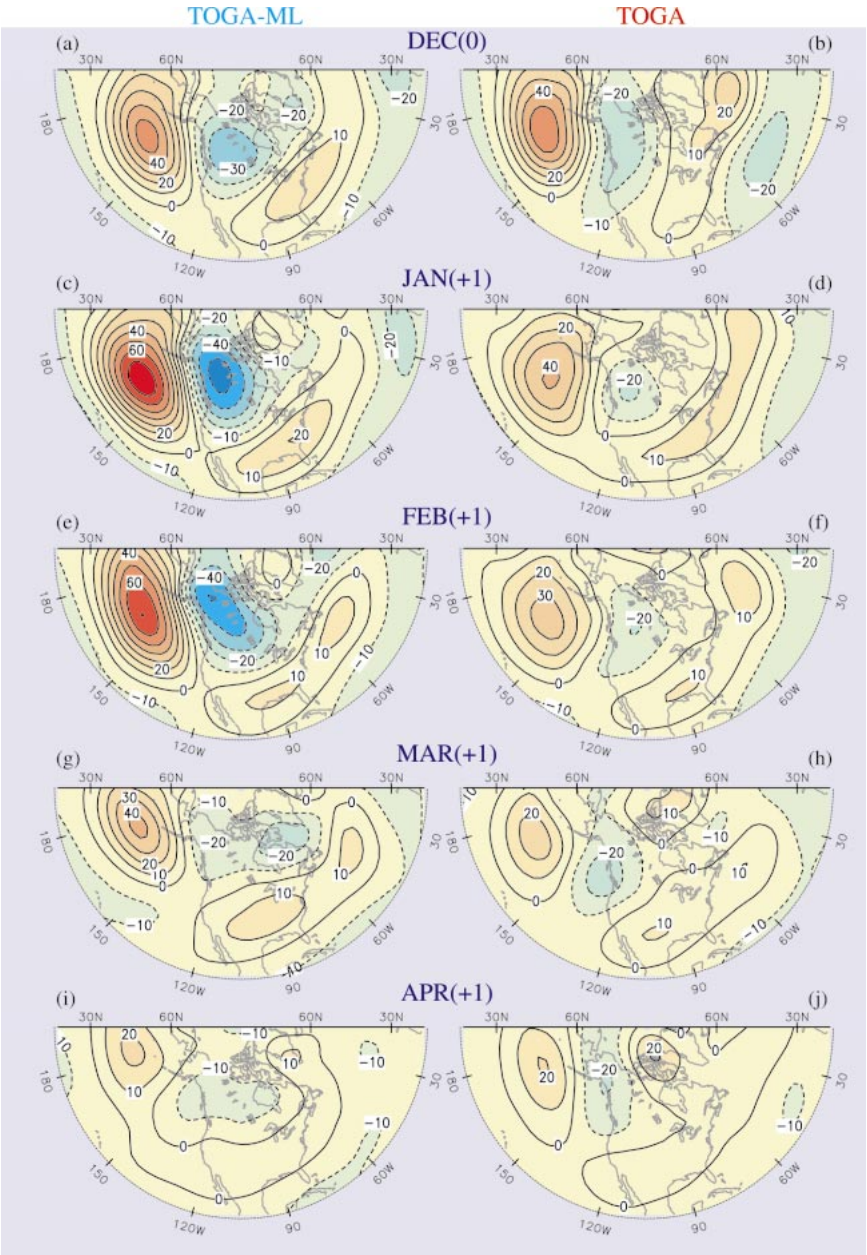

FIG. 11. As in Fig. 10, but for composites over eight cold ENSO events.

lated height anomalies is also comparable with that of the observed signals.

Inspection of the warm composite patterns based on TOGA data for individual months (right panels in Fig. 10) reveals that the amplitude of the cyclonic anomaly over the North Pacific remains almost constant throughout the period from December (0) to February (+1). Similarly, the TOGA-ML composites (left panels in Fig. 10) also indicate uniform strength of the Pacific anomaly through the winter months. The temporal evolution of the anomalous centers over North America and the western North Atlantic in TOGA is characterized by a distinct peak in amplitude in February (+1) (see Fig. 10f), with a period of steady growth in the preceding months, and followed by decay in spring. On the other hand, the strength of the corresponding anomalies in TOGA-ML persists for a relatively longer period. For instance, large positive height anomalies over Canada and southern Greenland are evident through the January–March (+1) period. Moreover, the negative anomaly over the Atlantic at ~40°N remains strong in March (+1) and April (+1), during which the amplitude of this feature in

TOGA-ML (Figs. 10g and 10i) exceeds that in TOGA (Figs. 10h and 10j) by more than a factor of 2.

The cold composite patterns for TOGA (right panels in Fig. 11) indicate that the intensity of the height anomalies in the North Pacific/western Canadian sector is highest in December (0), and undergoes a continuous attenuation from that month to April (+1). In contrast, the strength of the corresponding features in TOGA-ML (left panels in Fig. 11) is maintained from December (0) to February (+1). The maximum amplitude of these signals in TOGA-ML, attained in January–February (+1) (Figs. 11c and 11e), is twice as high as that simulated in TOGA for the same months (Figs. 11d and 11f). The anomalies over the western North Atlantic and the eastern seaboard of North America are weak in both TOGA-ML and TOGA throughout much of the composite period considered here.

In summary, the impact of additional sea–air feedback processes outside of the tropical Pacific (as inferred from differences between the TOGA-ML and TOGA results) is most discernible in the North Atlantic during March–April (+1) of the warm ENSO events (Figs. 10g–j), and in the North Pacific during January–February (+1) of the cold events (Figs. 11c–f). In both instances, the ''direct'' atmospheric response to ENSO, as simulated in TOGA, decays rapidly with time. On the other hand, the corresponding evolution of the TOGA-ML signals is characterized by a relatively stronger persistence from one month to the next. This finding is in accord with the model studies of Barsugli (1995) and Bladé (1997, 1999), who noted that sea–air coupling effectively reduces the thermal damping of the atmosphere, thus enhancing the temporal persistence of extratropical atmospheric signals.

In order to evaluate the extent to which the differences in amplitude between the TOGA-ML and TOGA features in Figs. 10–11 may be attributed to differences in the level of temporal variability in the two experiments, the anomalies appearing in the left and right panels of these figures have been normalized by the local standard deviation for the respective experiments. The distinctions between the TOGA-ML and TOGA composites, as noted in the preceding paragraphs, are equally apparent in the patterns for the standardized anomalies thus computed (not shown). Hence the above comparison of the TOGA-ML and TOGA signals is not sensitive to the variance characteristics of the two experiments.

b. TOGA-ML versus TOGA: Difference charts

To examine in greater detail the differences in the atmospheric circulation simulated in TOGA-ML and TOGA, and to assess the statistical significance of such differences, the composite anomalies of selected variables in TOGA have been subtracted from the corresponding fields in TOGA-ML. The difference charts thus obtained are displayed in Fig. 12, for the Pacific sector in January–February (+1) of cold ENSO events (left panels), and the Atlantic sector in March–April (+1) of warm ENSO events (right panels). As demonstrated in Figs. 10–11, differences between the two experiments are largest during these specific months in the respective ocean sectors. The variables presented in Fig. 12 include (top panels) 500-mb height, (middle panels) sea level pressure (SLP), and (lower panels) surface wind vectors (arrows) and SST (shading).

The confidence level of the signals displayed in Fig. 12 has been evaluated using the technique described in Chervin and Schneider [1976, Eqs. (2)–(3)]. This method entails the computation of a t value, which is the ratio of the difference between TOGA-ML and TOGA to a measure of the variance of the data samples used in constructing the composites. The latter quantity encompasses variability of the anomalies appearing in each of the four individual runs, and in each of the eight ENSO warm or cold events considered in this study. For the 500-mb height and SLP fields (Figs. 12a–d), the significance levels as estimated by this procedure are indicated by green shading of various densities. It is seen that the principal extrema in these panels surpass the 95% confidence limit. For the surface wind vectors (Figs. 12e,f), those grid points with either the zonal or meridional components exceeding the 90% significance level are highlighted using bold arrows.

There exists considerable spatial resemblance between the difference charts for 500-mb height and the corresponding composite patterns based on TOGA-ML and TOGA separately (cf. Fig. 12a with Figs. 11c–f; and Fig. 12b with Figs. 10g–j). Hence these difference charts primarily portray the amplification of the signals in TOGA-ML relative to those in TOGA. An analogous conclusion can be drawn by comparing the surface wind vectors in Figs. 12e and 12f with the corresponding regression charts in Figs. 3a and 7a, respectively. Inspection of the difference patterns in SLP (Figs. 12c,d) reveals substantial spatial displacement of the near-surface features from those in the midtroposphere (Figs. 12a–d), especially in the Alaska–western Canada and Greenland–Iceland sectors.

To explore the potential role of sea–air feedbacks in modulating the extratropical response to ENSO forcing, we next consider the extent to which the differences between TOGA-ML and TOGA may be attributed to forcing from the North Pacific and North Atlantic SST anomalies as indicated by shading in Figs. 12e,f. Advances in our understanding of this issue have thus far been impeded by the disparate results reported in various model studies (see recent review by Robinson 2000). Simulated responses to prescribed extratropical SST forcing are seen to depend on many details of experimental design, such as placement and polarity of the SST anomaly, background flow, sampling methodology, model numerics, and so on.

Sensitivity experiments have been conducted by Ferranti et al. (1994), Peng et al. (1995, 1997), Rodwell et

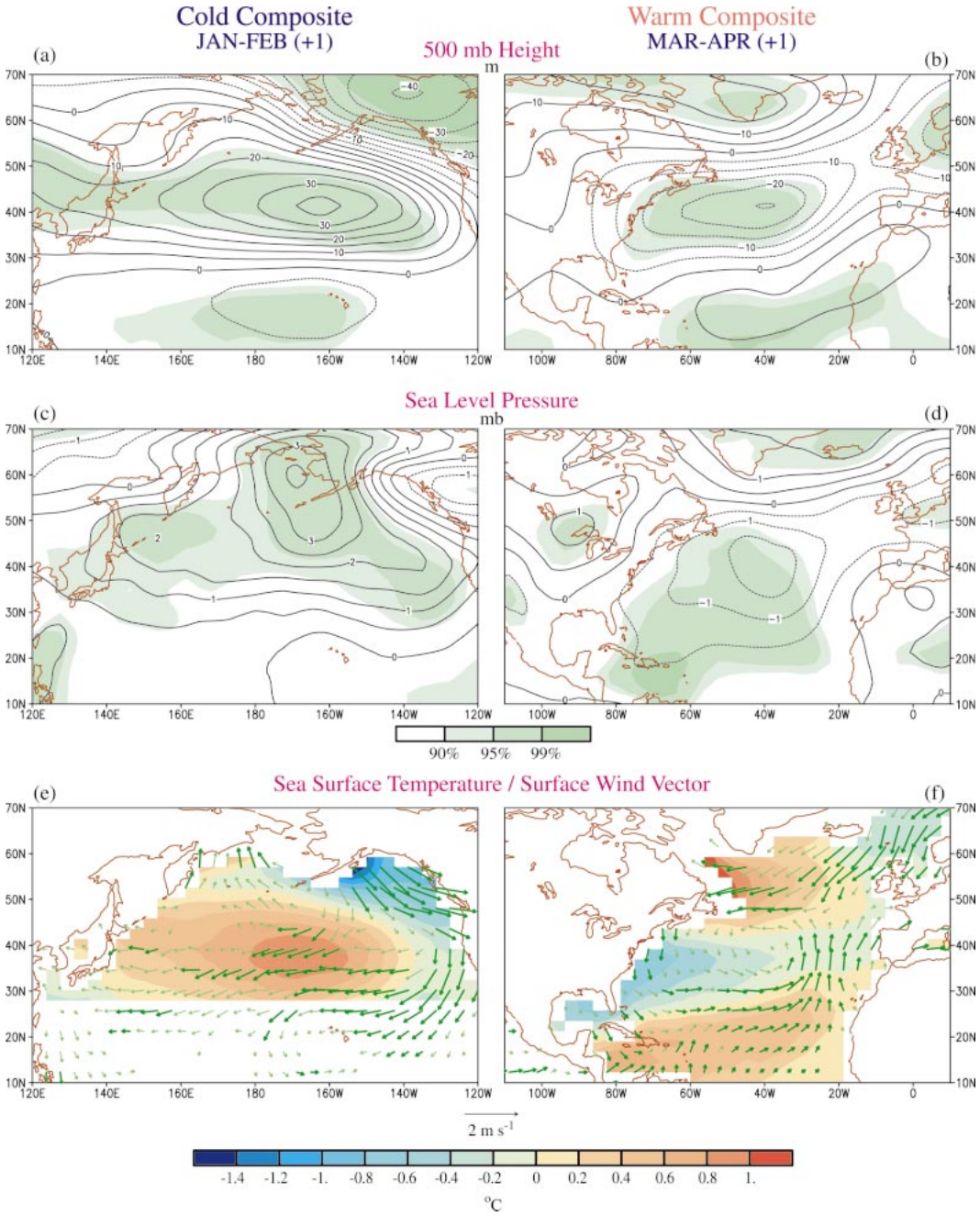

FIG. 12. Difference patterns as obtained by subtracting the four-run averaged composite fields for TOGA from the corresponding fields for TOGA-ML: (left) cold composites in Jan–Feb (+1); (right) warm composites in Mar–Apr (+1); (top) 500-mb height (contours, interval: 5 m); (middle) sea level pressure (contours, interval: 0.5 mb); (bottom) sea surface temperature (shading, see scale bar at bottom) and surface wind vectors (see scale at bottom). The statistical significance of the features in (a)–(d) is indicated using green shading (see scale bar below middle panels). Wind vectors in (e) and (f) with either the zonal or meridional component exceeding the 90% significance level are highlighted using bold green arrows. Vectors not meeting this criterion are plotted in thin green arrows.

al. (1999), and Venzke et al. (1999), among others, by prescribing SST anomalies over various portions of the North Pacific and North Atlantic. The spatial relationships between SST forcing and model response noted in some of these studies are consistent with those depicted in Fig. 12. The potential role of sea–air feedbacks is further reinforced by findings based on the coupled GCM experiments analyzed by Delworth (1996), Grötzner et al. (1998), and Saravanan (1998). These studies indicate that the leading modes of coupled variability

over the North Atlantic and North Pacific are characterized by atmospheric patterns similar to Figs. 12a–d, and SST patterns resembling Figs. 12e,f.

6. Summary and discussions

Results from the TOGA-ML experiment indicate considerable sensitivity of the SST conditions in both the North Pacific and North Atlantic to ENSO forcing in the tropical Pacific. The temporal lag of extratropical SST anomalies relative to the ENSO forcing (Figs. 1 and 6), as well as the salient roles of ENSO-related atmospheric anomalies in driving the extratropical ocean mixed layer (Figs. 3 and 7), confirm the impacts of ENSO on SST variability at various sites in the northern oceans through the atmospheric bridge mechanism. Regression statistics of SST and selected atmospheric fields near the ocean surface, as computed using output from TOGA-ML, are in good agreement with observations. The advantages of using a higher (R30) resolution in the current study than the R15 runs examined previously are apparent from the almost twofold increase in the amplitudes of the oceanic and atmospheric signals presented here (e.g., compare the SST and geopotential height charts in Figs. 1, 6, 10, and 11 of this study with the corresponding results in Figs. 8 and 12 in LN96 based on the R15 version).

Detailed diagnosis of the surface heat budgets at selected sites in the North Pacific and North Atlantic during individual months (Figs. 4, 5, and 8) reveals strong seasonal dependence of various components of the surface heat fluxes. Anomalous wind speeds typically peak in January–February (+1), thus resulting in prominent contributions of the terms $-C_S V' \Delta\overline{T}$ and $-C_L V' \Delta\overline{q}$ in that period. Variations in T'_o and q'_o tend to lag those in T'_a and q'_a by 1–2 months, so that the composite time series for the oceanic and atmospheric anomalies in temperature or humidity (see pertinent red and blue curves in Figs. 4, 5, and 8) intersect each other in February–April (+1). In the months preceding this crossover point, the sea–air gradients $\Delta T'$ and $\Delta q'$ are such that the terms $-C_S \overline{V} \Delta T'$ and $-C_L \overline{V} \Delta q'$ have the same polarity as the concurrent T'_o. In the period after the intersection, both $\Delta T'$ and $\Delta q'$ change sign, and the same terms oppose the SST signal. Anomalous shortwave radiative fluxes contribute strongly to the surface heat budgets at the subtropical sites D and E during the winter months (see Figs. 8h and 8l).

The evidence presented in section 5 suggests that sea–air coupling over the North Pacific and Atlantic may affect the local atmospheric response to ENSO through the following:

- Enhanced temporal persistence of the atmospheric anomaly, due to attenuation of thermal damping associated with an ocean mixed layer with finite heat capacity (see discussion in section 5a).
- Driving of the atmospheric circulation by midlatitude SST anomalies generated by the atmospheric bridge (see discussion in section 5b).

Further model experimentation and data diagnosis are needed to ascertain the relative contributions of increased persistence versus dynamical sea–air feedbacks to ENSO-related variability of the extratropical coupled system.

The impact of ocean–atmosphere interactions on the atmospheric signals, as deduced from differences between the composite charts based on the TOGA-ML and TOGA experiments (Figs. 10–12), is seen to exhibit a notable dependence on the polarity of ENSO events, ocean basin, and seasonal timing. Such dependencies may partially be attributed to the following factors:

- Comparison of the ''direct'' atmospheric responses to warm and cold ENSO events (as inferred from TOGA output, see right panels of Figs. 10–11), reveals that, in addition to a sign reversal, the principal anomalies in the warm and cold composites also differ considerably in amplitude and spatial pattern. Some of these differences could be linked to disparities between the tropical Pacific precipitation anomalies (and the attendant diabatic forcing) occurring in the warm and cold events considered here. For instance, the TOGA composite charts for precipitation rate (not shown) indicate that the amplitude of the enhanced precipitation over the central equatorial Pacific remains high throughout the period from December (0) to March (+1) during warm events, whereas the strength of the corresponding (negative) anomalies in the cold events undergoes a steady decline from December (0) to March (+1). The distinct temporal evolution of the tropical diabatic heating during warm and cold episodes may account for the prolonged appearance of the extratropical atmospheric response in the warm composites for 500-mb height (right panels of Fig. 10), and the noticeable decay in strength of the corresponding signals in the cold composites (right panels of Fig. 11). The nonlinear characteristics of rainfall anomalies in El Niño and La Niña episodes, and their implications on extratropical teleconnections, have previously been studied by Hoerling et al. (1997).
- Midlatitude sea–air interactions could be dependent on the strength of the local wind circulation, which is related to the polarity of the ambient geopotential height anomalies. Model results presented by Webster (1981) indicate that weak zonal background flows allow for a stronger coupling between the atmospheric circulation and the local heating or cooling due to SST anomalies (i.e., the system approaches the ''diabatic limit''). Conversely, when strong basic wind conditions prevail, the system is in the ''advective limit,'' with thermal advection by the horizontal flow playing a dominant role, and local coupling between the SST anomaly and the atmospheric circulation becoming much weaker. Held and Ting (1990) have similarly noted that the atmospheric response to extra-

tropical heating decreases as the strength of the low-level flow increases. The findings of our study are in accord with these results: the effects of ocean–atmosphere coupling is most evident near Site A in the cold composite (Fig. 11), and near Site C in the warm composite (Fig. 10). In both instances, the SST anomaly at Sites A or C is sandwiched between a positive geopotential height anomaly to the north and a negative anomaly to the south, so that the strength of the prevalent westerlies at the SST site itself is reduced, and the system is closer to the diabatic limit.

- The impact of sea–air interaction on the atmospheric signal over the Atlantic is most discernible in March–April (+1) of warm events (Fig. 10). The seasonal timing of strong coupling in this sector may be related to that of the direct atmospheric response to ENSO in the Atlantic region (as inferred from TOGA output). It is seen from Fig. 10f that the latter response does not attain maximum amplitude until February (+1). The somewhat delayed occurrence of the Atlantic height anomalies (relative to those over the Pacific) may in part be linked to the temporal evolution of the eastward-propagating Rossby wave train over the extratropical Western Hemisphere, as noted in the observational study by Honda et al. (2001). Another contributing factor to the seasonal timing of sea–air coupling in the Atlantic is that the ENSO-driven SST anomalies at various Atlantic sites are strongest in March–April (+1) (see top panels of Fig. 8). Hence, it is during this phase of the seasonal cycle that these SST anomalies are most effective in influencing the local atmospheric circulation.

This study presents evidence on teleconnections between ENSO forcing in the tropical Pacific and SST changes not only in the North Pacific, but also in the North Atlantic. The covariability of SST in the near-equatorial and north temperate portions of the Pacific basin has been thoroughly documented in previous investigations. The more remote link between ENSO and the North Atlantic has thus far received less attention. The possibility of other atmospheric bridges connecting ENSO events to the tropical Atlantic and Indian Oceans (as described by Enfield and Mayer 1997 and Klein et al. 1999), as well as to the southern oceans, also needs to be explored.

Whereas the emphasis of the present study is on the linkages between ENSO and the surface conditions of extratropical oceans, it is noteworthy that SST changes in the tropical Pacific account for only a fraction of the SST variance in the North Pacific and North Atlantic. For instance, the singular value decomposition analysis presented in Fig. 9 of LN96 indicates that tropical Pacific SST forcing explains 35% and 56% of the observed and R15-simulated North Pacific SST variability, respectively. Furthermore, Deser and Blackmon (1995) have identified a SST pattern in the North Pacific that is independent of ENSO. There is hence a considerable amount of SST variability in midlatitude oceans that cannot be attributed to ENSO processes. To gain a comprehensive understanding of extratropical ocean variability, it is necessary to take into consideration remote ENSO influences as well as other mechanisms operating within the temperate zone.

In view of our findings on the seasonal timing of various atmospheric and oceanic signals, the detailed seasonal dependence of various facets of sea–air interaction related to ENSO needs to be taken into account in future investigations. These studies would benefit from simulations using an ocean mixed layer model with a variable depth (e.g., Alexander et al. 2000). This model improvement would not only yield more realistic geographical and seasonal dependence of the thermal capacity of the surface ocean, but would also allow for temporary sequestration of heat energy below the thermocline (Alexander and Deser 1995). The latter process could result in a longer-term memory of the ocean system, and may contribute to coupled sea–air variability on timescales much longer than those (i.e., several months) considered here.

The evidence presented in section 5 demonstrates that much can be learned about the nature of extratropical ocean–atmosphere feedbacks by examining the differences between the simulations in TOGA-ML and TOGA. Ensemble runs with still larger sample sizes are necessary to assess the robustness of these results. Integrations using other GCMs and experimental designs would also serve as independent checks on different aspects of the atmospheric bridge mechanism as reported in the present study.

Experimentation with an atmospheric GCM coupled to an ocean mixed layer model with variable depth is currently under way. The number of parallel runs for a given SST forcing scenario is to be increased from the present 4 to 8 or even 16. Results from this new suite of integrations will be reported in the future.

Acknowledgments. We thank Ileana Bladé and Mike Alexander for stimulating discussions and expert advice in the course of this study. The insightful comments by them as well as Steve Klein, John Lanzante, and Joel Norris on a preliminary version of this manuscript have been very helpful in the drafting process. Incorporation of the constructive suggestions by Yochanan Kushnir and another official reviewer has resulted in clarification of some of the issues addressed in this work. This work is part of a NOAA–Universities collaborative effort for model diagnosis. Support of this effort by the NOAA Climate and Global Change Program is gratefully acknowledged.

REFERENCES

Alexander, M. A., 1990: Simulation of the response of the North Pacific Ocean to the anomalous atmospheric circulation associated with El Niño. *Climate Dyn.,* **5,** 53–65.

——, 1992a: Midlatitude atmosphere–ocean interaction during El Niño. Part I: The North Pacific Ocean. *J. Climate,* **5,** 944–958.
——, 1992b: Midlatitude atmosphere–ocean interaction during El Niño. Part II: The Northern Hemisphere atmosphere. *J. Climate,* **5,** 959–972.
——, and C. Deser, 1995: A mechanism for the recurrence of wintertime midlatitude SST anomalies. *J. Phys. Oceanogr.,* **25,** 122–137.
——, and J. D. Scott, 1995: *Atlas of Climatology and Variability in the GFDL R30S14 GCM.* CIRES, University of Colorado, 121 pp. [Available from the authors at CDC/NOAA, R/E/CD1, 325 Broadway, Boulder, CO 80303-3328.]
——, and ——, 1997: Surface flux variability over the North Pacific and North Atlantic Oceans. *J. Climate,* **10,** 2963–2978.
——, ——, and C. Deser, 2000: Processes that influence sea surface temperature and ocean mixed depth variability in a coupled model. *J. Geophys. Res.,* **105,** 16 823–16 842.
Barsugli, J. J., 1995: Idealized models of intrinsic midlatitude atmosphere–ocean interaction. Ph.D. dissertation, University of Washington, 187 pp. [Available from Dept. of Atmospheric Sciences, University of Washington, Box 351640, Seattle, WA 98195-1640; or online at http://www.cdc.noaa.gov/~jjb/thesis.html.]
Bladé, I., 1997: The influence of midlatitude ocean–atmosphere coupling on the low-frequency variability of a GCM. Part I: No tropical SST forcing. *J. Climate,* **10,** 2087–2106.
——, 1999: The influence of midlatitude ocean–atmosphere coupling on the low-frequency variability of a GCM. Part II: Interannual variability induced by tropical SST forcing. *J. Climate,* **12,** 21–45.
Broccoli, A. J., and S. Manabe, 1992: The effects of orography on midlatitude Northern Hemisphere dry climates. *J. Climate,* **5,** 1181–1201.
Cayan, D. R., 1992a: Latent and sensible heat flux anomalies over the northern oceans: The connection to monthly atmospheric circulation. *J. Climate,* **5,** 354–369.
——, 1992b: Latent and sensible heat flux anomalies over the northern oceans: Driving the sea surface temperature. *J. Phys. Oceanogr.,* **22,** 859–881.
Chervin, R. M., and S. H. Schneider, 1976: On determining the statistical significance of climate experiments with general circulation models. *J. Atmos. Sci.,* **33,** 405–412.
Curtis, S., and S. Hastenrath, 1995: Forcing of anomalous sea surface temperature evolution in the tropical Atlantic during Pacific warm events. *J. Geophys. Res.,* **100,** 15 835–15 847.
DaSilva, A., A. C. Young, and S. Levitus, 1994: *Atlas of Surface Marine Data 1994.* Vols. 1–5. NOAA Atlas NESDIS 6–10, 1636 pp.
Delworth, T. L., 1996: North Atlantic interannual variability in a coupled ocean–atmosphere model. *J. Climate,* **9,** 2356–2375.
Deser, C., and M. L. Blackmon, 1993: Surface climate variations over the North Atlantic Ocean during winter: 1900–1989. *J. Climate,* **6,** 1743–1753.
——, and ——, 1995: On the relationship between tropical and North Pacific sea surface temperature variations. *J. Climate,* **8,** 1677–1680.
Enfield, D. B., and D. A. Mayer, 1997: Tropical Atlantic sea surface temperature variability and its relation to El Niño–Southern Oscillation. *J. Geophys. Res.,* **102,** 929–945.
Ferranti, L., F. Molteni, and T. N. Palmer, 1994: Impact of localized tropical and extratropical SST anomalies in ensembles of seasonal GCM integrations. *Quart. J. Roy. Meteor. Soc.,* **120,** 1613–1645.
Gordon, C. T., and W. F. Stern, 1982: A description of the GFDL global spectral model. *Mon. Wea. Rev.,* **110,** 625–644.
Grötzner, A., M. Latif, and T. P. Barnett, 1998: A decadal climate cycle in the North Atlantic Ocean as simulated by the ECHO coupled GCM. *J. Climate,* **11,** 831–847.
Held, I. M., and M. Ting, 1990: Orographic versus thermal forcing of stationary waves: The importance of the mean low-level wind. *J. Atmos. Sci.,* **47,** 495–500.
Hoerling, M. P., A. Kumar, and M. Zhong, 1997: El Niño, La Niña, and the nonlinearity of their teleconnections. *J. Climate,* **10,** 1769–1786.
Honda, M., H. Nakamura, J. Ukita, I. Kousaka, and K. Takeuchi, 2001: Interannual seesaw between the Aleutian and Icelandic lows. Part I: Seasonal dependence and life cycle. *J. Climate,* **14,** 1029–1042.
Hsiung, J., and R. E. Newell, 1983: The principal nonseasonal modes of variation of global sea surface temperature. *J. Phys. Oceanogr.,* **13,** 1957–1967.
Klein, S. A., B. J. Soden, and N.-C. Lau, 1999: Remote sea surface temperature variations during ENSO: Evidence for a tropical atmospheric bridge. *J. Climate,* **12,** 917–932.
Lau, N.-C., and M. J. Nath, 1996: The role of the ''atmospheric bridge'' in linking tropical Pacific ENSO events to extratropical SST anomalies. *J. Climate,* **9,** 2036–2057.
Levitus, S., 1982: *Climatological Atlas of the World Ocean.* NOAA Professional Paper 13, 173 pp. [Available from Superintendent of Documents, U.S. Government Printing Office, Washington, DC 20402.]
Luksch, U., and H. von Storch, 1992: Modeling the low-frequency sea surface temperature variability in the North Pacific. *J. Climate,* **5,** 893–906.
Manabe, S., R. J. Stouffer, M. J. Spelman, and K. Bryan, 1991: Transient responses of a coupled ocean–atmosphere model to gradual changes of atmospheric CO_2. Part I: Annual mean responses. *J. Climate,* **4,** 785–818.
Miller, A. J., D. R. Cayan, T. P. Barnett, N. E. Graham, and J. M. Oberhuber, 1994: Interdecadal variability of the Pacific Ocean: Model response to observed heat flux and wind stress anomalies. *Climate Dyn.,* **9,** 287–302.
Namias, J., and D. R. Cayan, 1981: Large-scale air–sea interactions and short period climate fluctuations. *Science,* **214,** 869–876.
Pan, Y. H., and A. H. Oort, 1990: Correlation analyses between sea surface temperature anomalies in the eastern equatorial Pacific and the World Ocean. *Climate Dyn.,* **4,** 191–205.
Peng, S., L. A. Mysak, H. Ritchie, J. Derome, and B. Dugas, 1995: The differences between early and midwinter atmospheric response to sea surface temperature anomalies in the northwest Atlantic. *J. Climate,* **8,** 137–157.
——, W. A. Robinson, and M. P. Hoerling, 1997: The modeled atmospheric response to midlatitude SST anomalies and its dependence on background circulation states. *J. Climate,* **10,** 971–987.
Robinson, W. A., 2000: Review of WETS—The Workshop on Extra-Tropical SST Anomalies. *Bull. Amer. Meteor. Soc.,* **81,** 567–577.
Rodwell, M. J., D. P. Rowell, and C. K. Folland, 1999: Oceanic forcing of the wintertime North Atlantic oscillation and European climate. *Nature,* **398,** 320–323.
Saravanan, R., 1998: Atmospheric low-frequency variability and its relationship to midlatitude SST variability: Studies using the NCAR Climate System Model. *J. Climate,* **11,** 1386–1404.
Seager, R., Y. Kushnir, M. Visbeck, N. Naik, J. Miller, G. Krahmann, and H. Cullen, 2000: Causes of Atlantic Ocean climate variability between 1958 and 1998. *J. Climate,* **13,** 2845–2862.
Smith, T. M., R. W. Reynolds, R. E. Livezey, and D. C. Stokes, 1996: Reconstruction of historical sea surface temperatures using empirical orthogonal functions. *J. Climate,* **9,** 1403–1420.
Trenberth, K. E., 1997: The definition of El Niño. *Bull. Amer. Meteor. Soc.,* **78,** 2771–2777.
——, G. W. Branstator, D. Karoly, A. Kumar, N.-C. Lau, and C. Ropelewski, 1998: Progress during TOGA in understanding and modeling global teleconnections associated with tropical sea surface temperatures. *J. Geophys. Res.,* **103,** 14 291–14 324.
Venzke, S., M. R. Allen, R. T. Sutton, and D. P. Rowell, 1999: The atmospheric response over the North Atlantic to decadal changes in sea surface temperature. *J. Climate,* **12,** 2562–2584.
Wallace, J. M., C. Smith, and Q. Jiang, 1990: Spatial patterns of

atmosphere–ocean interaction in the northern winter. *J. Climate*, **3,** 990–998.

Weare, B. C., A. Navato, and R. E. Newell, 1976: Empirical orthogonal analysis of Pacific Ocean sea surface temperatures. *J. Phys. Oceanogr.*, **6,** 671–678.

Webster, P. J., 1981: Mechanisms determining the atmospheric response to sea surface temperature anomalies. *J. Atmos. Sci.,* **38,** 554–571.

Woodruff, S. D., R. J. Slutz, R. L. Jenne, and P. M. Steurer, 1987: A comprehensive ocean–atmosphere data set. *Bull. Amer. Meteor. Soc.*, **68,** 1239–1250.